Modulation of the Human Pancreatic Ductal Adenocarcinoma Immune Microenvironment by Stereotactic Body Radiotherapy

Bradley N. Mills[1], Haoming Qiu[2,3], Michael G. Drage[4], Chunmo Chen[4], Jocelyn S. Mathew[1], Jesse Garrett-Larsen[1], Jian Ye[1], Taylor P. Uccello[5], Joseph D. Murphy[5], Brian A. Belt[1], Edith M. Lord[3,5], Alan W. Katz[2,3], David C. Linehan[1,3], and Scott A. Gerber[1,3,5]

ABSTRACT

Purpose: Stereotactic body radiotherapy (SBRT) is an emerging treatment modality for pancreatic ductal adenocarcinoma (PDAC), which can effectively prime cytotoxic T cells by inducing immunogenic tumor cell death in preclinical models. SBRT effects on human PDAC have yet to be thoroughly investigated; therefore, this study aimed to characterize immunomodulation in the human PDAC tumor microenvironment following therapy.

Experimental Design: Tumor samples were obtained from patients with resectable PDAC. Radiotherapy was delivered a median of 7 days prior to surgical resection, and sections were analyzed by multiplex IHC (mIHC), RNA sequencing, and T-cell receptor sequencing (TCR-seq).

Results: Analysis of SBRT-treated tumor tissue indicated reduced tumor cell density and increased immunogenic cell

death relative to untreated controls. Radiotherapy promoted collagen deposition; however, vasculature was unaffected and spatial analyses lacked evidence of T-cell sequestration. Conversely, SBRT resulted in fewer tertiary lymphoid structures and failed to lessen or reprogram abundant immune suppressor populations. Higher percentages of PD-1+ T cells were observed following SBRT, and a subset of tumors displayed more clonal T-cell repertoires.

Conclusions: These findings suggest that SBRT augmentation of antitumor immunogenicity may be dampened by an overabundance of refractory immunosuppressive populations, and support the continued development of SBRT/immunotherapy combination for human PDAC.

Introduction

The high prevalence of metastatic disease at the time of pancreatic ductal adenocarcinoma (PDAC) diagnosis has bolstered dismal 5-year survival rates of less than 10% (1). Highly immunosuppressive features of the PDAC tumor microenvironment (TME), including a dense desmoplastic stroma that contains a predominance of tumor-supportive myeloid cells (2, 3), further drives therapeutic inefficacy. In addition, tumor-associated fibroblasts deposit a complex extracellular matrix (ECM) of hyaluronic acid and collagen that leads to profound hypovascularity (4). Both ECM sequestration and poor vascular perfusion may limit T-cell infiltration into tumor nests, excluding them to peritumoral regions and ectopic lymphoid organizations known as tertiary lymphoid structures (TLS; refs. 5, 6).

Although immunotherapy has shown efficacy for various hematologic tumors, several malignancies, including PDAC, remain treatment refractory. Accordingly, combination immunotherapy

approaches that employ an immune-priming combination have become a focal point of frontline treatment strategies. Therapies that directly damage malignant cells promote the release of various peptides including tumor neoantigens and damage-associated molecular patterns (DAMP) that can potentially educate and prime antitumor immune responses (7). Clinical trials for PDAC have investigated various agents to stimulate immunogenic cell death (ICD), including chemotherapy (8–10), radiotherapy (11), radiofrequency ablation (12), and irreversible electroporation (13), with varying degrees of success.

Stereotactic body radiotherapy (SBRT) is an emerging local treatment modality for PDAC that minimizes damage to surrounding normal tissues and can spare lymphocytes by precisely delivering radioeffective doses (25–40 Gy) in three to five oligofractions (14, 15). The accuracy and timing of SBRT delivery is essential for antitumor effects, as its therapeutic efficacy is dependent upon CD8 T-cell infiltration and cytolytic activity (16). In murine PDAC models, SBRT has been shown to induce ICD and promote tumor cell antigen presentation, resulting in the augmentation of tumor-reactive T cells (17). Conversely, radiotherapy responses can also suppress antitumor immunity by recruiting Tregs (18) and myeloid suppressors (19), reinforcing the immune-suppressive phenotypes of stromal cells (20), and upregulating programmed death-ligand 1 (PD-L1) expression on tumor cells to promote T-cell exhaustion (21). These immunosuppressive features of the radioresponse likely contribute to the lack of improved overall survival observed in the clinical treatment of PDAC (22). Although preclinical studies have demonstrated that SBRT can effectively recruit and prime cytotoxic T cells, the efficiency of immune stimulation in human PDAC, given its uniquely immunosuppressive TME, has yet to be investigated.

This study aimed to characterize immunomodulation in the human PDAC TME following preoperative SBRT. Analysis of

[1]Department of Surgery, University of Rochester Medical Center, Rochester, New York. [2]Department of Radiation Oncology, University of Rochester Medical Center, Rochester, New York. [3]Wilmot Cancer Institute, University of Rochester Medical Center, Rochester, New York. [4]Department of Pathology and Laboratory Medicine, University of Rochester Medical Center, Rochester, New York. [5]Department of Microbiology and Immunology, University of Rochester Medical Center, Rochester, New York.

Corresponding Author: Scott A. Gerber, Department of Surgery, University of Rochester Medical Center, 601 Elmwood Avenue, Rochester, NY 14642. E-mail: scott_gerber@urmc.rochester.edu

Translational Relevance

The clinical data provided in this work characterizes the PDAC immune microenvironment following SBRT, identifying aspects of both immunogenic transformation and residual immunosuppression. Although SBRT has no significant impact on PDAC survival outcomes, these findings indicate that radiation elicits ICD, augments the intratumoral ratio of activated T cells, and supports the enrichment of tumor-reactive T-cell clones in a subset of patients. Despite evidence of antitumor immune priming, intratumoral T-cell levels remain characteristically low, and lymphocytes are shown to be outnumbered by treatment refractory myeloid suppressors by approximately 100:1. This work provides evidence that SBRT can initiate an antitumor immunogenic response against human PDAC, reinforcing its utility as a combination with immunotherapy. Furthermore, the identification of residual immunosuppressive components serves to inform continued development of multimodal approaches to reverse this barrier.

SBRT-treated tumor tissue (a median of 7 days posttreatment) using multiplex IHC (mIHC), total RNA sequencing (RNA-seq), and T-cell receptor β-chain sequencing (TCR-seq) highlighted both immune-stimulatory modulation as well as residual nodes of tumor-supportive immunosuppression. Importantly, radiotherapy reduced PDAC cell density and induced ICD without collateral damage to vasculature. Coordinate spatial analyses provided no evidence of impaired T-cell migration from vessels or sequestration in dense collagen deposits resulting from radiation. Our findings argue that the chief barrier to SBRT-induced antitumor immune responses in PDAC is an overabundance of immunosuppressive myeloid populations. Although intratumoral percentages of PD-1$^+$ T cells were increased by SBRT and more clonal T-cell repertoires were observed, the ratio of myeloid suppressors to T cells neared 100:1. These findings collectively suggest that SBRT may indeed initiate antitumor immune responses against human PDAC, however, survival benefits are likely abrogated by enduring immune suppression mechanisms in the TME. Accordingly, while SBRT lacks efficacy as a monotherapy, this work demonstrates its potential as a combination for immunotherapy interventions.

Materials and Methods

Patients

Histologic examination was used to diagnose pancreatic head adenocarcinoma that was designated as resectable by National Comprehensive Cancer Network (NCCN) guidelines in eligible patients (ages 18 and older, all sexes). Main inclusion criteria included no radiographic evidence of superior mesenteric or portal vein distortion, no evidence of distant metastasis, no enlarged lymph nodes per CT criteria or lymphadenopathy, Karnofsky performance status >70, and adequate bone marrow function. Main exclusion criteria included prior surgical resection of any pancreatic malignancy, prior invasive malignancy (except non-melanomatous skin cancer) unless disease free for a minimum of 3 years, any prior chemotherapy or radiation for treatment of the patient's pancreatic tumor, severe and active comorbidity, and pregnancy or childbearing potential. Adjuvant treatment was administered per medical oncology. Comparison samples for the nonrandomized study were identified through a query of the University of Rochester Medical Center (URMC) Department of Surgical

Pathology database, and obtained separately, and subject demographics can be found in Supplementary Table S1.

Stereotactic body radiotherapy

For treatment planning, CT simulation with ExacTrac body markers was used for respiratory gating. If placed, gold fiducials were used for image-guided radiation therapy (IGRT). Twenty-five Gy in five fractions was prescribed to the planning target volume (PTV), defined as gross tumor plus a margin of 3 to 5 mm to limit potential toxicity, chiefly fibrosis. Pancreaticoduodenectomy was performed a median of 7 days following the completion of SBRT. Resected PDAC tissue was processed for histology (FFPE, 5 μm sections) by the URMC Department of Surgical Pathology for downstream analyses similar to those employed in previous characterizations of the treatment-naïve PDAC TME (6).

RNA-seq

Tissue scrolls were generated from 5 μm sections of resected human PDAC tissue. Sample processing, library preparation, and sequencing was performed by MedGenome. Briefly, a SMARTer Stranded Total RNA-seq Pico Input Kit (Takara) was used for library prep, and 80M total reads were captured using a NovaSeq 6000 (Illumina) platform. Reads mapping to the ribosomal and mitochondrial genome were removed before performing STAR (RRID:SCR_004463) alignment. Raw read counts were estimated using HTSeq (RRID:SCR_005514), and normalized using DESeq2 (RRID:SCR_000154) to get the normalized counts. Cufflinks (RRID:SCR_014597) was used for estimating expression from aligned reads. Fold changes in differentially-expressed genes were calculated from FPKM values.

For pathway analyses, over representation analysis (ORA) using the Kyoto Encyclopedia of Genes and Genomes (KEGG) Pathway Database (RRID:SCR_012773) and Gene Set Enrichment Analysis (GSEA, C2: curated genesets; refs. 23–27) was performed to identify significant differentially-expressed protein coding from RNA-seq data. Computational analyses were performed using the R Bioconductor (RRID: SCR_006442) package clusterProfiler (RRID:SCR_016884). ORA plots were generated using the WEB-based GEne SeT AnaLysis Toolkit (WebGestalt; ref. 28). The OncoPeptTUME in silico platform was utilized for macrophage polarization analyses. Signature-based scoring was calculated using the single sample GSEA (ssGSEA) method provided by the ESTIMATE R package. RNA-seq detailed quality control was performed using RNA-SeQC (RRID:SCR_005120), RSeQC (RRID:SCR_005275), and MultiQC (RRID:SCR_014982).

mIHC

mIHC staining was performed by the Experimental Histopathology Shared Resource of the Fred Hutch/University of Washington Cancer Consortium. FFPE PDAC slides were baked for 1 hour at 60°C, then dewaxed and stained on a Leica BOND Rx stainer using Leica Bond reagents for dewaxing (Dewax Solution). MOTiF 6-plex antibody panels were designed to assess myeloid, lymphoid, and structural (Supplementary Table S1) cell populations. Antigen retrieval/antibody stripping (Epitope Retrieval Solution 2) and rinsing was performed after each step (Bond Wash Solution). Antigen retrieval and antibody stripping steps were performed at 100°C with all other steps at ambient temperature.

Endogenous peroxidase activity was blocked with 3% H_2O_2 for 5 minutes followed by protein blocking with TCT buffer (0.05M Tris, 0.15M NaCl, 0.25% Casein, 0.1% Tween 20, 0.05% ProClin300 pH 7.6) for 10 minutes. The first primary antibody (position 1) was applied for

60 minutes followed by the secondary antibody application for 10 minutes and the application of the tertiary TSA-amplification reagent (PerkinElmer OPAL fluor) for 10 minutes. A high stringency wash was performed after the secondary and tertiary applications using high-salt TBST solution (0.05M Tris, 0.3M NaCl, and 0.1% Tween-20, pH 7.2–7.6). Species-specific polymer HRP was used for all secondary applications, either Leica's PowerVision Poly-HRP anti-Rabbit Detection or anti-mouse detection. Primary and secondary antibodies were stripped with retrieval solution for 20 minutes before repeating the process with the second primary antibody (position 2) starting with a new application of 3% H_2O_2. The process was repeated until five positions were completed. For the sixth position, following the secondary antibody application, Opal TSA-DIG was applied for 10 minutes, followed by a 20-minute stripping step in retrieval solution and application of Opal 780 fluor for 10 minutes with high stringency washes performed after the secondary, TSA DIG, and Opal 780 fluor applications. The stripping step was not performed after the final position. Slides were removed from the stainer and stained with DAPI for 5 minutes, rinsed for 5 minutes, and coverslipped with Prolong Gold Antifade reagent (Invitrogen/Life Technologies).

Slides were cured overnight at room temperature, then whole slide images were acquired on the Vectra Polaris Quantitative Pathology Imaging System (Akoya Biosciences). The entire tissue was selected for processing using Phenochart and the images were spectrally unmixed using inForm software. Unmixed images were exported as multi-image TIF files, which were analyzed with HALO image analysis software (Indica Labs) using the High-Plex FL module. Cellular analysis of the images was performed by first identifying cells based on nuclear recognition (DAPI stain), then measuring fluorescence intensity of the estimated cytoplasmic areas of each cell. A mean intensity threshold above background was used to determine positivity for each fluorochrome within the cytoplasm, thereby, defining cells as either positive or negative for each marker. The positive cell data was then used to define colocalized populations. The HALO Classifier module was used to annotate regions of dense collagen, TLS, and tumor nests, via Random Forrest analysis. TLS cellular quantifications were performed on annotated TLS containing >500 total cells, and additionally, >100 CD8 T cells for $CD8^+PD-1^+$ quantification. The HALO Spatial Analysis module was used for spatial and proximity analyses.

Histology/IHC

Mayer's hematoxylin and eosin staining was performed on the leading section of each FFPE PDAC tissue series. Tumoral and adjacent peritumoral regions were annotated by a licensed pathologist.

HMGB-1 and HSP70 staining was used to assess DAMP levels on sequential sections. Briefly, PDAC sections were dewaxed with three 5-minute washes in xylenes. Samples were then rehydrated by 2-minute washes in 95% EtOH (x2), 80% EtOH, 70% EtOH, and H_2O, and endogenous peroxidase activity was blocked with a 30-minute incubation in 0.3% H_2O_2. Sections were incubated in blocking buffer (DAKO serum-free protein block) for 1 hour, followed by overnight primary antibody incubation in anti-HMGB1 (1:1,000, Abcam, Catalog No. ab18256, RRID:AB_444360) or anti-HSP70 (1:100, Abcam, Catalog No. ab2787, RRID:AB_303300). Secondary antibodies were applied with 30-minute incubations, followed by HRP/DAB (ABC) detection (Abcam). Slides were counterstained with hematoxylin (VDW).

Masson's trichrome staining was performed using the Trichrome, Masson, Aniline Blue Stain Kit (Newcomer Supply). Briefly, PDAC sections were dewaxed with three 5-minute washes in xylenes, and then rehydrated by washing in 95% EtOH (x2) and 80% EtOH (x2). Slides were incubated in Bouin's fluid overnight for dye fixation, followed by a 10-minute incubation in 1% hematoxylin to stain nuclei. Acidophilic tissue elements were stained with Biebrich Scarlet-Acid Fuchsin stain for 2 minutes, followed by decolorization for 15 minutes in phosphomolybdic-phosphotungstic acid and collagen staining for 5 minutes in Aniline Blue stain. Slides were then incubated in 0.5% acetic acid for five minutes to differentiate tissue sections.

Whole slide tissue sections were digitized and registered at 20× magnification using an Aperio VERSA Digital Histology System (Leica Biosystems) equipped for high-resolution whole slide scanning. Analyses were performed using Aperio ImageScope (RRID:SCR_014311). The Positive Pixel Count algorithm was used to quantify the total number of collagen-positive pixels (blue), as well as 1+ (low) and 2+ (moderate) DAMP-stained pixels (brown) in tumor and peritumor regions.

TCR-seq

Tissue scrolls were generated from 5 µm sections of resected human PDAC tissue. Genomic DNA extraction, library preparation, and survey level sequencing was performed by Adaptive Biotechnologies. Briefly, the ImmunoSEQ TCRβ Kit was used to generate sequencing libraries, utilizing a bias-controlled multiplex-PCR amplification of rearranged TCR CDR3 sequences that allowed for a quantitative readout of T-cell repertoires. Forward primers were targeted to the V segment of the TCR, and reverse primers targeted the J segment. Genomic DNA input provided CDR3 sequences that were highly representative of the relative frequency of each rearrangement in the sample population, capturing the full TCR repertoire including specific individual clones. Analyses were performed on the ImmunoSEQ Analyzer and ImmunoMap platforms (29). For ImmunoMap structural TCR repertoire analysis, sequencing data were filtered to include only sequences with >4 reads. Dominant motif analyses were run on the top 40% of sequences in each response, with the following input parameters: homology threshold = 0.3, cluster frequency threshold = 1, PAM10 scoring matrices, and gap penalty = 30.

Statistical analysis

GraphPad Prism 7 software (RRID:SCR_002798) was used for all statistical analyses, and P values of <0.05 were considered significant. For RNA-seq analyses, the significant differential expression cutoffs employed were P value <0.05 and fold change ≥ 2 or ≤ −2. Quantification analyses comparing untreated (UT) and SBRT-treated groups were tested for significance using two-tailed unpaired parametric t tests. For spatial and proximity analyses, each dataset was fit to a second-order polynomial equation using nonlinear least squares regression, and B0, B1, and B2 parameters were compared using an extra sum-of-squares F test to determine significance. Comparison of CD8 T-cell proximities to myeloid suppressor, Treg, and tumor cell populations was tested for significance using an ordinary two-way ANOVA and Tukey multiple comparisons test with a single pooled variance. PCA clustering of samples was performed on standardized loadings, and principal components with eigenvalues greater than 0.5 were selected. Significance for the quantification of TCR repertoire characteristics between untreated, immunologically "cold" SBRT, and immunogenically "hot" SBRT samples was calculated using an ordinary one-way ANOVA test with Holm–Sidak test for multiple comparisons.

Study approval

This single-arm pilot study of preoperative SBRT for resectable PDAC was conducted in accordance with recognized ethical guidelines stated in the Belmont Report, and approved by the URMC Institutional Review Board (NCT02347618). Written informed consent was obtained from all patients recruited for this study. Samples were deidentified prior to analysis for patient confidentiality and blinding. Patients and the public were not involved in the design, conduct, reporting, or dissemination plans of our research.

Data availability

The RNA-seq data generated during this study are available at NCBI Gene Expression Omnibus (GEO) under the accession number GSE185311. (https://www.ncbi.nlm.nih.gov/geo/query/acc.cgi?acc=GSE185311). TCR-seq data will be made available upon request to Scott A. Gerber (scott_gerber@urmc.rochester.edu).

Results

Patient characteristics and study design

Patients diagnosed with resectable PDAC were enrolled in a single-arm pilot study (NCT02347618) investigating preoperative SBRT ($n = 9$). Stereotactic body radiotherapy was delivered at a dose of 25 Gy over 5 consecutive days (5 Gy $\times$ 5), and patients underwent surgical resection a median of 7 days (2–14 days) following the final SBRT fraction. Comparison samples (untreated control) were obtained from patients with resectable PDAC who underwent routine surgical resection without any prior therapy ($n = 14$, Supplementary Table S1). The majority of tumors (65.2%) represented stage T1c and T2 malignancies with lymphovascular invasion (LVI, 73.9%), and only three (17.6%) demonstrated poor differentiation. No differences in overall survival were observed between untreated ($\overline{OS} = 29.6$ months) and SBRT-treated ($\overline{OS} = 29.1$ months) groups (Supplementary Fig. S1A), and progression-free survival in SBRT-treated patients ($\overline{PFS} = 24.0$ months) indicated modest increases relative to untreated controls ($\overline{PFS} = 10.4$ months, Supplementary Fig. S1B). All tumor samples used for correlative studies were FFPE from debulked tissue by the Surgical Pathology Department at the University of Rochester Medical Center. Sequential 5 μm sections from tumor blocks were used for subsequent RNA-seq, mIHC (Supplementary Table S2), and TCR-seq analyses of the tumor immune microenvironment.

SBRT reduces tumor burden and elicits ICD in PDAC

We assessed the magnitude of DNA damage and corresponding cell death in PDAC tumors targeted by SBRT, compared with unirradiated control. RNA-seq was used to examine gene signatures associated with apoptotic/necrotic radioresponses. Overrepresentation analysis was performed on differentially-expressed genes (DEG) between untreated (UT) and SBRT-treated samples, mapping to the KEGG Pathway Database. Results indicated significant over-representation of the TP53 signaling pathway (**Fig. 1A**). Furthermore, GSEA of DEGs identified the significant enrichment of TP53 DNA damage response (Supplementary Fig. S2A) and irradiation response (Supplementary Fig. S2B) genesets. The tumor protein P53 (P53) is a master regulator of the DNA damage response, controlling a myriad of genes involved in the regulation of cell-cycle arrest, DNA repair, metabolic adaptation, and cell death (30). Overall, these data indicate the general upregulation of DNA damage response signaling in PDAC tissue targeted by SBRT relative to untreated controls.

Distinct areas of tumor and adjacent peritumoral regions were annotated using an H&E stained leading section from each sample series by a licensed pathologist at the University of Rochester (Supplementary Fig. S2C). Nuclear staining (DAPI) of all cells in tumor regions identified reductions in overall cellularity following SBRT delivery (Supplementary Figs. S2D and S2E), and multiplex staining with pan-cytokeratin (pan-CK, AE1/AE3) revealed corresponding significant decreases in the tumor cell densities of SBRT-treated samples (**Fig. 1B** and **C**). Furthermore, cellular segmentation indicated reduced tumor cell nuclear roundness following SBRT, suggesting a prevalence of damaged and/or dying PDAC cells (Supplementary Fig. S2F; ref. 31). To assess levels of ICD, sections were stained for two DAMPs: high-mobility group box 1 protein (HMGB1) and HSP70. IHC analysis revealed cumulative increases in weak staining surrounding densely stained cell nuclei and cytoplasm in SBRT-treated samples, characteristic of the cytoplasmic and extracellular release of nuclear HMGB1 and cellular HSP70 (32, 33), respectively, during ICD (**Fig. 1D–F**; Supplementary Fig. S2G). These results collectively argue that SBRT directly induces ICD in the PDAC TME that, importantly, can persist throughout the week(s) following treatment.

Collagen deposition in SBRT-treated PDAC does not increase T-cell sequestration

Radiotherapy has been shown to promote fibrosis (34), and radiation-induced fibrotic deposition in PDAC may promote therapeutic resistance and disease progression by preventing effector T-cell infiltration (35, 36). To assess the onset of fibrosis in resectable PDAC following SBRT, we stained tissue sections with Masson's trichrome to visualize collagen density. Our results indicated that SBRT treatment significantly augments collagen deposition throughout tissue sections within days following SBRT (**Fig. 2A** and **B**). To assess the potential for cell sequestration in fibrotic regions, we performed a spatial analysis of T-cell abundances within or beyond dense collagen interfaces annotated using a tissue classifier machine learning algorithm (**Fig. 2C–E**). Although SBRT-treated tumors contained more collagen, fewer CD8^{+} (**Fig. 2F** and **G**) and CD4^{+} (**Fig. 2H** and **I**) T cells were found to reside within areas of dense collagen relative to untreated controls. Accordingly, these results indicate that although collagen deposition was induced by SBRT, it did not promote T-cell sequestration.

PDAC vasculature remains unchanged following SBRT

Proliferative endothelial cells (EC) in the TME can display radiosensitivity (37). Accordingly, radiotherapy has been shown to induce EC dysfunction and apoptosis, leading to reduced vascular density and hypoperfusion (38). We assessed PDAC vasculature following SBRT by staining for anti-CD31 (**Fig. 3A**), however our findings did not reveal any differences in EC number (**Fig. 3B**), vessel area (annotated using a tissue classifier machine learning algorithm, **Fig. 3C**), or vascular spatial density (**Fig. 3D** and **E**) between untreated and SBRT-treated tumors. Spatial analysis of relative CD8 T-cell abundances within, and adjacent to (<200 μm) CD31^{+}-classified vessels did indicate a different cellular distribution following SBRT (**Fig. 3F**), with significantly fewer CD8 T cells residing less than 40 μm from vessels (Supplementary Fig. S3A). CD4 T-cell distribution was found to be similar between control and SBRT groups (Supplementary Figs. S3B and S3C). Comprehensively, these results suggest that the structure and function of PDAC vasculature are unaffected by SBRT and capable of supporting immune cell infiltration during antitumor immune responses. Furthermore, CD8 T-cell migration away from vessels may be improved following SBRT treatment.
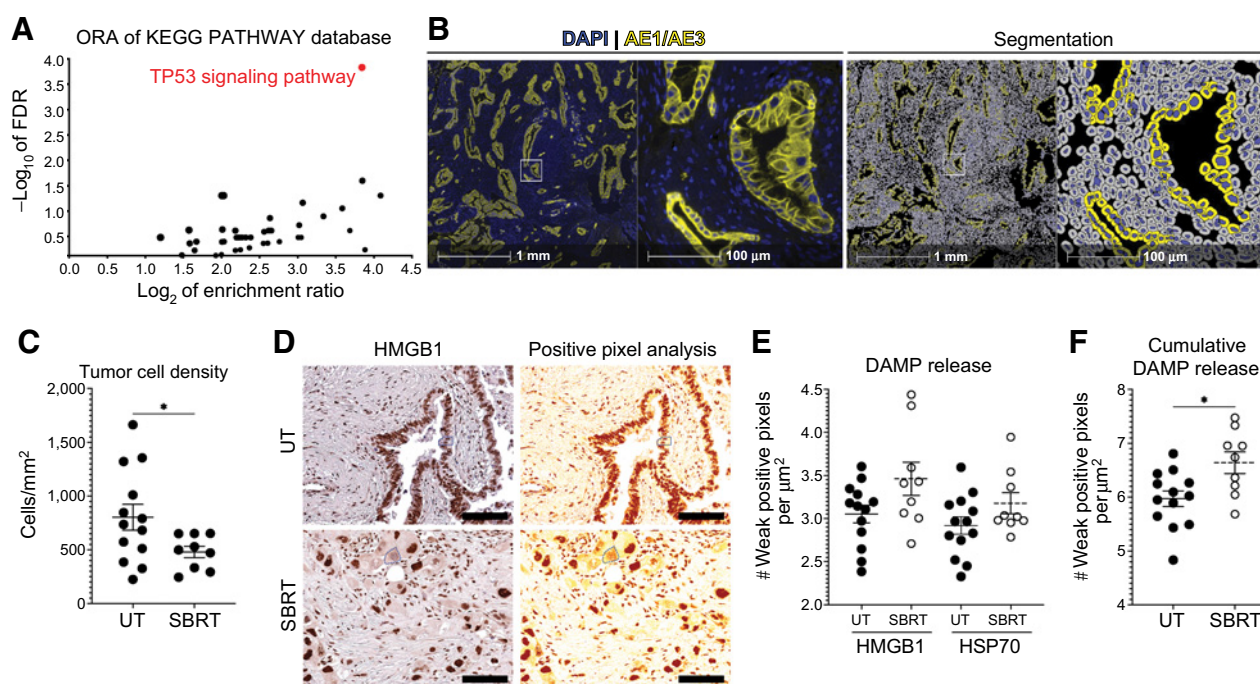
Figure 1.
SBRT reduces tumor burden and elicits ICD in PDAC. FFPE tissue sections from untreated control ($n = 14$) and SBRT-treated ($n = 9$) PDAC resections were FFPE for subsequent analyses. **A,** RNA-seq analysis was used to identify DEGs in SBRT-treated samples relative to controls. ORA was performed on DEGs mapped to the KEGG PATHWAY Database, and overrepresented pathways are plotted according to enrichment ratio ($\frac{\text{\# observed genes}}{\text{\# expected genes}}$) and FDR. **B** and **C,** Pan-Cytokeratin staining (AE1/AE3) was used to segment PDAC cells (**B,** representative images) for cell density quantification (**C**). White boxes in $4\times$ images indicate $20\times$ magnification ROI. **D–F,** HMGB1/HSP70 staining and positive pixel analysis (**D**, representative images) was used to quantify weak positive pixels (yellow/orange) indicative of cytoplasmic/extracellular DAMP release (**E**), and cumulative levels were assessed as a readout of overall ICD (**F**). Scale bar $= 100$ µm, $10\times$ magnification. For each analysis, statistical significance was determined by unpaired parametric t-tests. Data represent mean $\pm$ SEM (*, $P < 0.05$). See also Supplementary Fig. S2. UT $=$ untreated.

Irradiated PDAC TME demonstrates TLS remodeling

TLS organize during intraductal papillary mucinous neoplasm (IPMN) progression into PDAC, during which they accumulate immunosuppressive cell types (39). However, these satellite lymphoid organs may also serve crucial roles in tumor surveillance, and the presence of intratumoral TLS in PDAC has been associated with improved outcomes (5). Similar to primary lymph nodes, TLS are often predominantly composed of B cells that form distinct zones of aggregation (40). Accordingly, we annotated TLS structures using a tissue classifier machine learning algorithm to objectively identify CD19$^+$ B cell clusters across PDAC sections (**Fig. 4A**), and quantification of classified TLS revealed fewer structures in SBRT-treated sections relative to controls (**Fig. 4B**). Of note, no TLS were identified in four untreated and two SBRT-treated samples, resulting in sample sizes of 10 and 7, respectively, for subsequent TLS analyses. The structures present in SBRT-treated samples also exhibited a trend toward decreased average area (Supplementary Fig. S4A), however, a greater percentage were found to be located intratumorally or immediately adjacent to tumor regions (<500 µm) compared with untreated controls (**Fig. 4C**).

Next, mIHC was used to assess the overall densities of immune cell populations within TLS. For sampling accuracy, only sections with greater than 500 TLS-resident cells were analyzed (untreated $n = 7$, SBRT $n = 4$). No significant difference was observed in the levels of segmented CD11c$^+$HLA-DR$^+$CD68$^-$ dendritic cells (DC, Supplementary Figs. S4B and S4C) between untreated and SBRT-treated groups. Cellular segmentation was also used to identify regulatory Treg

(CD4$^+$FOXP3$^+$CD8$^-$), monocyte (CD14$^+$CD68$^-$CD15$^-$), macrophage (CD14$^+$CD68$^+$CD15$^-$), and granulocyte (CD15$^+$CD14$^-$CD68$^-$) populations within TLS (**Fig. 4D**), and results indicated that cumulative numbers of immunosuppressive cells were significantly lower in SBRT-treated TLS relative to untreated TLS (**Fig. 4E**). Corresponding analyses of CD8 T cells revealed no difference in cell density between groups (**Fig. 4F**; Supplementary Fig. S4D), however, the percentage of programmed death 1-positive (PD-1) CD8 T effector cells (in samples containing greater than 100 total CD8s) was significantly decreased following SBRT (**Fig. 4G**). Low numbers of CD4 T cells were identified in TLS following SBRT (Supplementary Fig. S4E). In summary, although SBRT was found to reduce the overall number and sizes of TLS in PDAC tissue, proximity to tumor nests and reduced immunosuppressive signatures argue antitumor immune supportive effects.

Intratumoral immunosuppressor populations persist following SBRT

Although SBRT can induce ICD, thereby priming antitumor immune responses, irradiation has also been shown to enhance both the recruitment of suppressor cells to the TME as well as augment the M2 immunosuppressive phenotype of intratumoral myeloid cells (20, 41). Using mIHC, we interrogated the levels of immunosuppressive cell types within PDAC intratumoral regions. Monocyte (**Fig. 5A**), macrophage (**Fig. 5B**), and granulocyte (**Fig. 5C**) populations displayed no differences in cell density, whereas Treg cells (**Fig. 5D**) were significantly decreased following
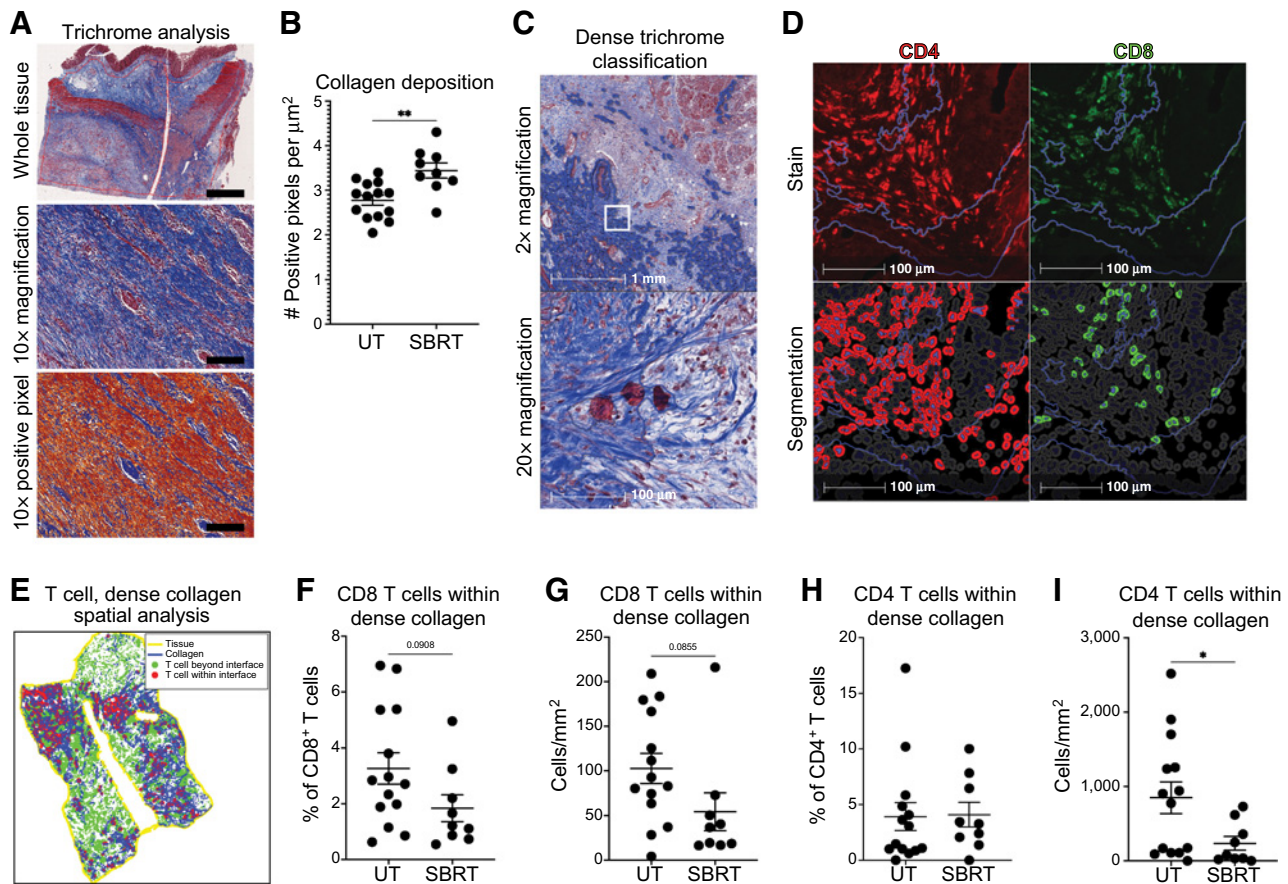
Figure 2.
Collagen deposition in SBRT-treated PDAC does not increase T-cell sequestration. **A** and **B,** Masson's trichrome staining and positive pixel analysis (**A**, representative images) was used to quantify collagen deposition (**B**). Scale bar = whole tissue = 2 mm, 10x = 200 μm. **C–I,** Regions of dense collagen were annotated using a tissue classifier machine learning algorithm (**C**, representative images), T cells within annotations were segmented from mIHC staining (**D**, representative images), and spatial analysis was performed (**E**, representative plot) to quantify the levels of CD8 (**F**: percentage, **G**: density) and CD4 (**H**: percentage, **I**: density) T cells within dense collagen. Blue lines annotate regions of dense collagen. For each analysis, statistical significance was determined by unpaired parametric t tests. Data represent mean ± SEM (*, $P < 0.05$; **, $P < 0.01$).

SBRT. In addition, OncoPeptTUME mapping of RNA-seq data provided evidence of conserved macrophage M1/M2 polarization between control and SBRT-treated groups across whole tissue sections (**Fig. 5E**).

In addition to stromal immune suppressors, PDAC tumor cells can also drive immunosuppression both indirectly (42) and directly (43). For example, radiation can augment the PD-L1/PD-1 axis by upregulating PD-L1 expression on tumor cells and dampening coordinate immune responses (44). mIHC assessment of pan-CK$^+$ tumor cells (**Fig. 5F**) revealed significant increases in PD-L1 expression following SBRT (**Fig. 5G**). No significant increase was observed collectively across all other cell types (Supplementary Fig. S5A). In addition, PDAC cells from SBRT-treated samples did not display a coordinate upregulation of MHC I (**Fig. 5H**), indicating an immunosuppressive bias in classical phenotypic response. These studies collectively suggest that SBRT does not augment or repolarize the myeloid immunosuppressor compartment in PDAC, however, reductions in suppressive Treg cells indicate an element of proinflammatory transformation. Alternatively, refractory tumor cells may be driven toward a state that supports immune escape.

T-cell activation in SBRT-treated PDAC contends with prevalent suppressor cell burden

We determined if SBRT treatment of PDAC tumors generates an antitumor immune response by using mIHC and RNA-seq. IHC analysis of intratumoral T-cell distribution revealed nonsignificant reductions in both CD8 and CD4 densities between untreated and SBRT-treated PDAC tissues (**Fig. 6A**; Supplementary Figs. S6A and S6B, respectively). Of note, no intratumoral CD4 T cells were identified in two untreated and two SBRT-treated samples, resulting in sample sizes of 12 and 7, respectively, for subsequent intratumoral CD4 T-cell analyses. Interestingly, levels of the PD-1$^+$ effector subtypes were found to be significantly augmented by SBRT treatment (**Fig. 6B**). A tissue classifier machine learning algorithm was used to annotate tumor nests based on pan-CK staining patterns (**Fig. 6C**). Results revealed a trend toward increased CD8 T-cell densities within tumor nests of SBRT-treated samples relative to controls (**Fig. 6D**), however, no clear differences in CD4 T-cell abundance were observed (Supplementary Fig. S6C). Separately, mIHC segmentation of intratumoral DCs indicated a trend of reduced density following SBRT (Supplementary Fig. S6D).
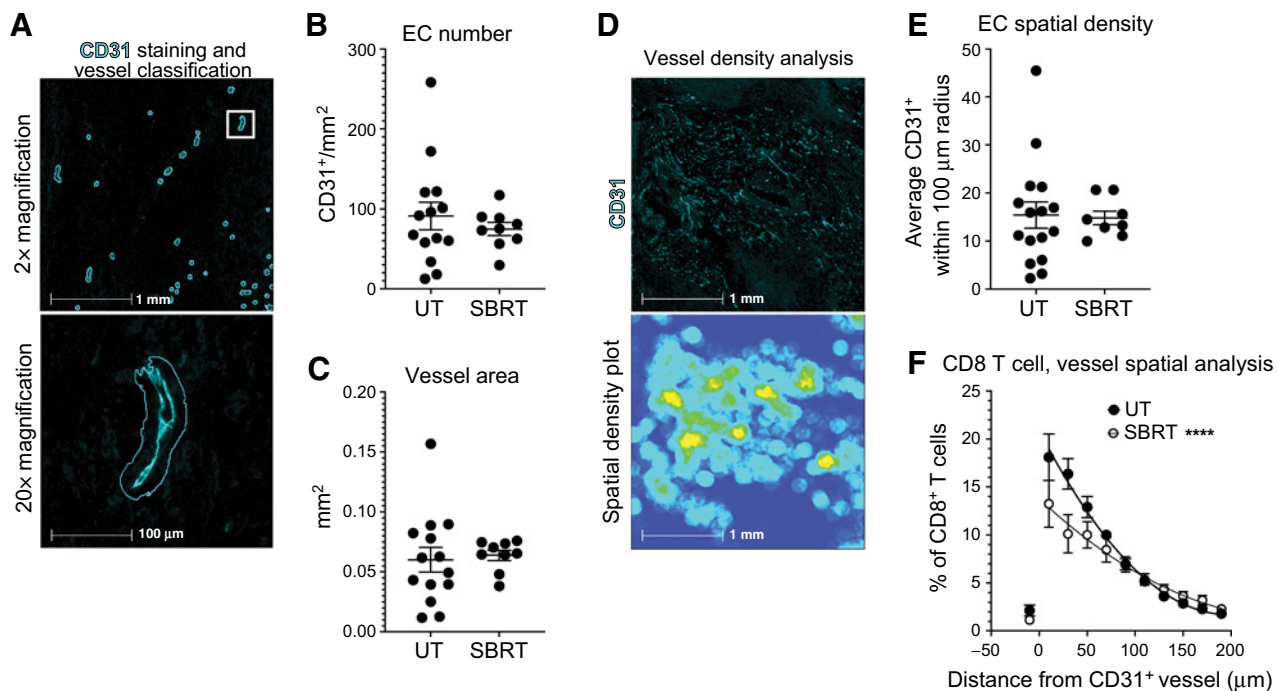
Figure 3.
PDAC vasculature remains unchanged following SBRT. **A–C,** CD31 staining/segmentation and a tissue classifier algorithm was used to annotate vessels (**A**, representative images) and quantify EC density (**B**) and vessel area (**C**). Cyan lines annotate vessels. **D** and **E,** Spatial density analysis of CD31 staining (**D**, representative images) and quantification of EC spatial density (**E**). Cyan/Green/Yellow = low/mid/high CD31 stain density, respectively. **F,** CD8 T cells were segmented from mIHC staining and spatial distribution analysis relative to vessels was performed. For each analysis, statistical significance was determined by unpaired parametric t tests. Data represent mean ± SEM (****, $P < 0.0001$). See also Supplementary Fig. S3.

Although SBRT treatment was found to augment the relative levels of PD-1$^+$ T cells in the PDAC TME, myeloid suppressor recalcitrance could still suppress antitumor potential. Accordingly, mIHC was used to evaluate the spatial relationship between PD-1$^+$ T cells and suppressive myeloid (monocyte, macrophage, granulocyte) populations (**Fig. 6E**). Our findings confirmed marked suppressor:CD8 T-cell ratios (approximately 100:1) in the SBRT treatment cohort, slightly greater than untreated controls (**Fig. 6F**). Furthermore, proximity analyses indicated that CD8 T-cell proximity to myeloid suppressors, Treg cells, and tumor cells was not significantly affected by SBRT; however, the average distance to myeloid suppressors (approximately 15–30 µm) was markedly less than distances to Tregs (approximately 80–120 µm) and tumor cells (approximately 110–120 µm; **Fig. 6G**; Supplementary Fig. S6E), with greater than 90% of CD8 T cells residing within 50 µm of a suppressor cell in all samples (Supplementary Fig. S6F). CD4 T cells were found to maintain analogous spatial relationships to myeloid suppressor cells (Supplementary Figs. S6G–S6J). Comprehensively, these findings indicate that SBRT treatment augments the percentage of PD-1$^+$ T effectors in PDAC tumor regions; however, the number and functional capacity of these effectors are likely restrained by overwhelming myeloid suppressor burden.

SBRT induces clonal T-cell expansion in a subset of human PDAC tumors

Although intratumoral T-cell numbers following SBRT were comparable with untreated samples, SBRT-induced ICD can alter the clonal signature of the repertoire (45–47). T-cell receptor sequencing revealed no significant differences in the number of TCR β-chain rearrangements (Supplementary Fig. S6K), frequency of top clono-types (Supplementary Fig. S6L), or Simpson's clonality of T-cell repertoires (**Fig. 7A**) in SBRT-treated samples relative to control. Similarly, no differences were observed in the cumulative frequencies of top 500 clonotypes between groups (**Fig. 7B**); however, a subset of SBRT-treated samples displayed a trend toward increased frequency of top clonotypes (**Fig. 7C**). For further investigation of this population, we employed the ImmunoMap bioinformatics platform (29), which utilizes sequence relatedness and frequency information to assess TCR structural diversity beyond the scope of traditional mathematical constructs. Briefly, ImmunoMap uses hierarchical clustering to group structurally homologous TCR sequences that meet a user-defined frequency threshold, defined as dominant motifs. SBRT-treated samples representing trends of increased top clonotype frequency similarly displayed weighted repertoire dendrograms distinct from other SBRT and untreated samples (**Fig. 7D**). Collectively, SBRT treatment was found to produce trends of fewer dominant motifs (**Fig. 7E**) that made up a greater frequency of the T-cell repertoire (Supplementary Fig. S6M), and led to lower TCR diversity scores (**Fig. 7F**).

The variance in TCR diversity observed within the SBRT group suggests that the samples examined exhibited tumor-specific treatment responsiveness. Principal component analysis was used to classify samples based on immunogenicity, grouping tumors into immunologically "hot" or "cold" subsets. Datasets from our analyses of cumulative DAMP release, intratumoral myeloid suppressor density, and intratumoral PD-1$^+$ CD8 T effector percentage were loaded as regression variables, and principal component biplots displayed a prevailing group of untreated and SBRT-treated samples that were classified as immunogenically "cold." In addition, a spatially exclusive cluster of three SBRT-treated samples was also identified. These
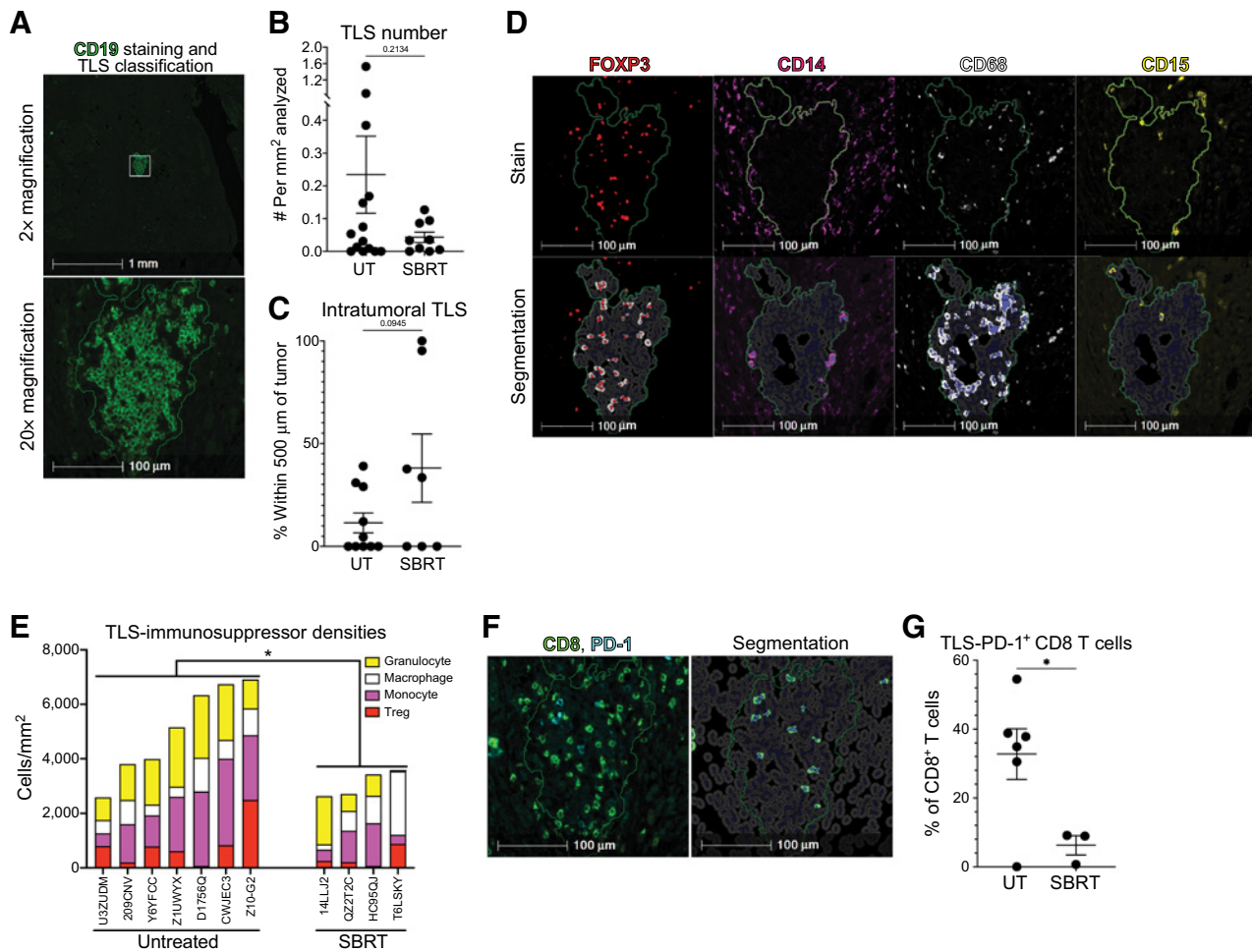
Figure 4.
Irradiated PDAC TME demonstrates TLS remodeling. **A–C,** CD19 staining/segmentation and a tissue classifier algorithm was used to annotate TLS (**A**, representative images) and quantify TLS number (**B**) and intratumoral percentages (**C**). Green lines annotate TLS. **D** and **E,** Treg (FOXP3^{+}), monocyte (CD14^{+}), macrophage (CD68^{+}), and granulocyte (CD15^{+}) cells were segmented from mIHC staining (**D**, representative images) and immunosuppressor levels within TLS were quantified (**E**). Statistics were performed on cumulative cell densities. **F** and **G,** PD-1^{+} CD8 T cells were segmented from mIHC staining (**F**) for quantification as a percentage of total CD8 T cells (**G**). For each analysis, statistical significance was determined by unpaired parametric t tests. Data represent mean $\pm$ SEM (*, $P < 0.05$). See also Supplementary Fig. S4.

samples were found to contain comparatively high levels of DAMP release, augmented PD-1^{+} CD8 T effector percentages, and low myeloid suppressor densities, and were classified as immunologically "hot" (**Fig. 7G**). We reassessed TCR repertoire characteristics based on the PCA plot immunogenic subsetting. Immunologically "hot" samples contained significantly fewer dominant motifs (**Fig. 7H**) and have significantly lower TCR diversity scores (**Fig. 7I**) relative to immunologically "cold" untreated and SBRT-treated groups. In addition, dominant motifs from the "hot" subset comprised a greater percentage of the overall T-cell repertoire relative to "cold" tumors (Supplementary Fig. S6N). Overall, these findings argue that SBRT is capable of generating a clonal T-cell response against a subset of treatment-responsive PDAC tumors.

Discussion

Stereotactic body radiotherapy is a standard treatment for various malignancies; however, immunologically "cold" tumors such as PDAC

are often refractory, and lack survival benefit (22, 37). The ability of radiotherapy to prime an antitumor immune response has been well established in animal models of PDAC (16, 48); nonetheless, the prominence of immunosuppressive stroma in human tumors may result in poor clinical translation. Accordingly, we hypothesized that SBRT initiates an antitumor response in human PDAC, independent of patient outcomes. Our investigation utilized a pilot study of preoperative SBRT for resectable PDAC, through which we acquired invaluable tissue samples that: (i) received only SBRT treatment, and (ii) were resected within a short period of time following therapy (2–14 days). Despite limited sample sizes, our data indeed described significant differences in several components of the antitumor immune response in PDAC tissues following SBRT. Notably, we report augmented tumor cell death independent of immune-restrictive modulation of the vasculature and ECM. Although SBRT increased the percentages PD-1^{+} T effector infiltrate in tumor regions, we did not observe favorable T-cell densities, or consistent clonal T-cell responses across the treatment cohort. Residual immune suppressor
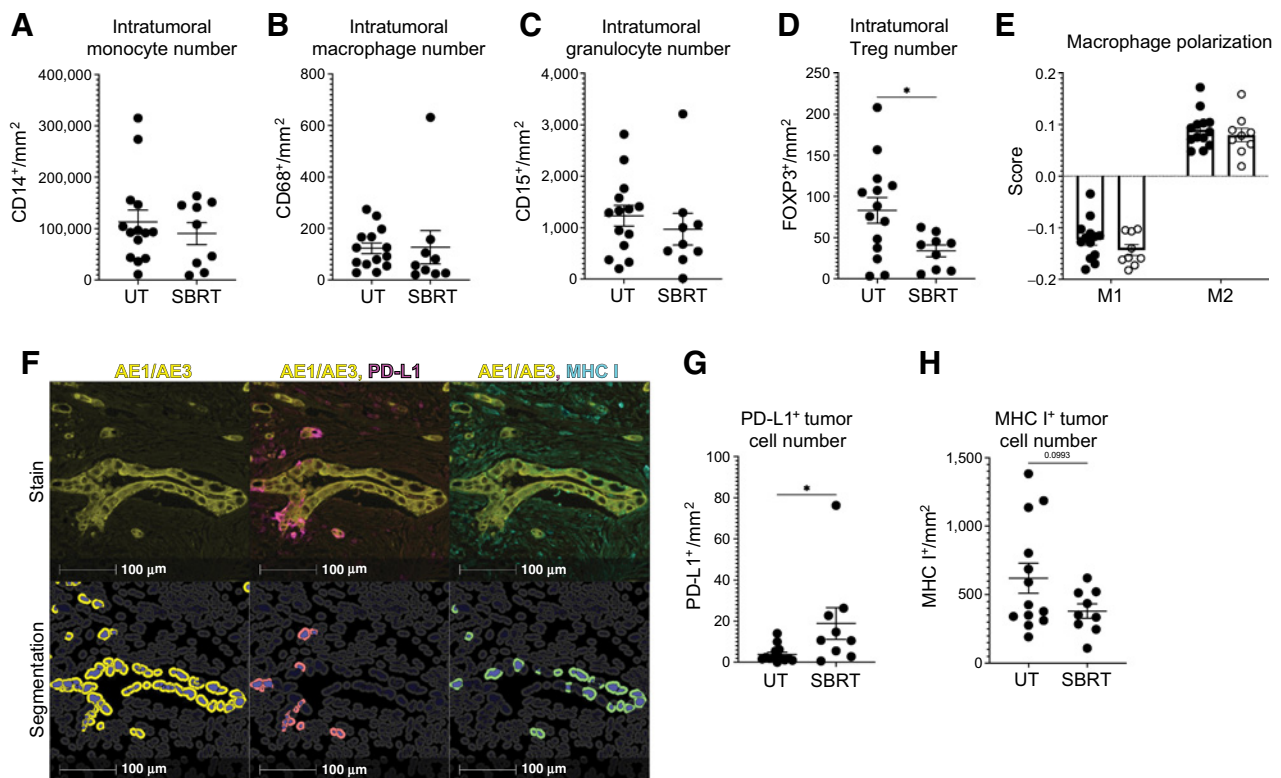
Figure 5.
Intratumoral immunosuppressor populations in PDAC persist following SBRT. **A–D,** Monocyte (**A**), macrophage (**B**), granulocyte (**C**), and Treg (**D**) cells were segmented from mIHC staining and intratumoral densities were quantified. **E,** OncoPeptTUME mapping of myeloid cell gene signatures from RNA-seq data were used for relative M1/M2 polarization scoring. **F–H,** Pan-Cytokeratin (AE1/AE3), PD-L1, and MHC I staining and segmentation (**F**, representative images) was used to quantify PD-L1$^+$ (**G**) and MHC I$^+$ (**H**) PDAC cells. For each analysis, statistical significance was determined by unpaired parametric t tests. Data represent mean $\pm$ SEM (*, $P < 0.05$). See also Supplementary Fig. S5.

cells and tumor cell escape mechanisms likely contributed to this finding, leading to variability in immunogenic responses. Comprehensively, these findings validate the importance of augmenting SBRT responses with complementary interventions, highlight the therapeutic potential for SBRT-centric immunotherapy combinations, and give insight regarding the refractory components within the human PDAC TME.

The PDAC TME is comprised of several features including fibroblasts, immune cells, ECs, and ECM, which serve critical roles in tumor initiation, progression, and radiation response. Advancements in the field of radiobiology have led to the emergence of several theories regarding which of these factors ultimately drive tumor regression following radiation-induced damage. For years, it was widely accepted that the antitumor effects following radiation were primarily governed by damage to ECs resulting in vascular collapse (49–51). This viewpoint was supported by observations that the linear quadratic model for calculating isoeffective radiation doses cannot account for therapeutic efficacy alone, and therefore, mechanisms apart from DNA damage to tumor cells must contribute to antitumor responses (52, 53). In addition, preclinical findings demonstrating progressive increases in tumor cell death in the days following a single fraction of high-dose irradiation suggested a secondary, indirect, mechanism characterized by reduced blood perfusion and increased hypoxia (54). Conversely, a subsequent study by Moding and colleagues found that altering cell death pathways in ECs had no effect on radiation-induced cell death in genetically engineered mouse sarcoma models; however, deletion of

the ATM radioresistance gene in tumor cells enhanced sarcoma eradication (55). Our findings demonstrate that the treatment of human PDAC with SBRT results in direct tumor cell killing (revisit **Fig. 1**), independent of observable effects on EC viability, vascular innervation, or vessel integrity (revisit **Fig. 3**). As clinical studies continue to explore the efficacy of novel radiation dosing and fractionation schemes, further investigation of indirect effects on vasculature, as well as perfusion studies, should be performed to develop a more comprehensive understanding of the therapeutic mechanism specific to PDAC.

Surprisingly, one of the most robust effects observed in the PDAC TME following SBRT was the reduction and remodeling of TLS (revisit **Fig. 4**). Although existing literature would suggest that decreases in PDAC TLS number would portend poor survival, increased percentages of intratumoral TLS in SBRT-treated samples could be beneficial. The origins and timing of intratumoral TLS development are beyond the scope of this study; however, given the decreased size of structures following SBRT (revisit Supplementary Fig. S4), we postulate that radiation damage may eradicate preexisting TLS, allowing for the *de novo* organization of aggregates within tumor regions. Importantly, the composition of TLS present in SBRT-treated tissues demonstrated a significant reduction in both myeloid and Treg immunosuppressor populations, representing a context supportive of CD8 T-cell activation and proliferation. Although we report SBRT-driven reductions in TLS- and dLN-resident PD-1$^+$ CD8 T cells, we believe this indicates increased tumoral trafficking of antigen-specific
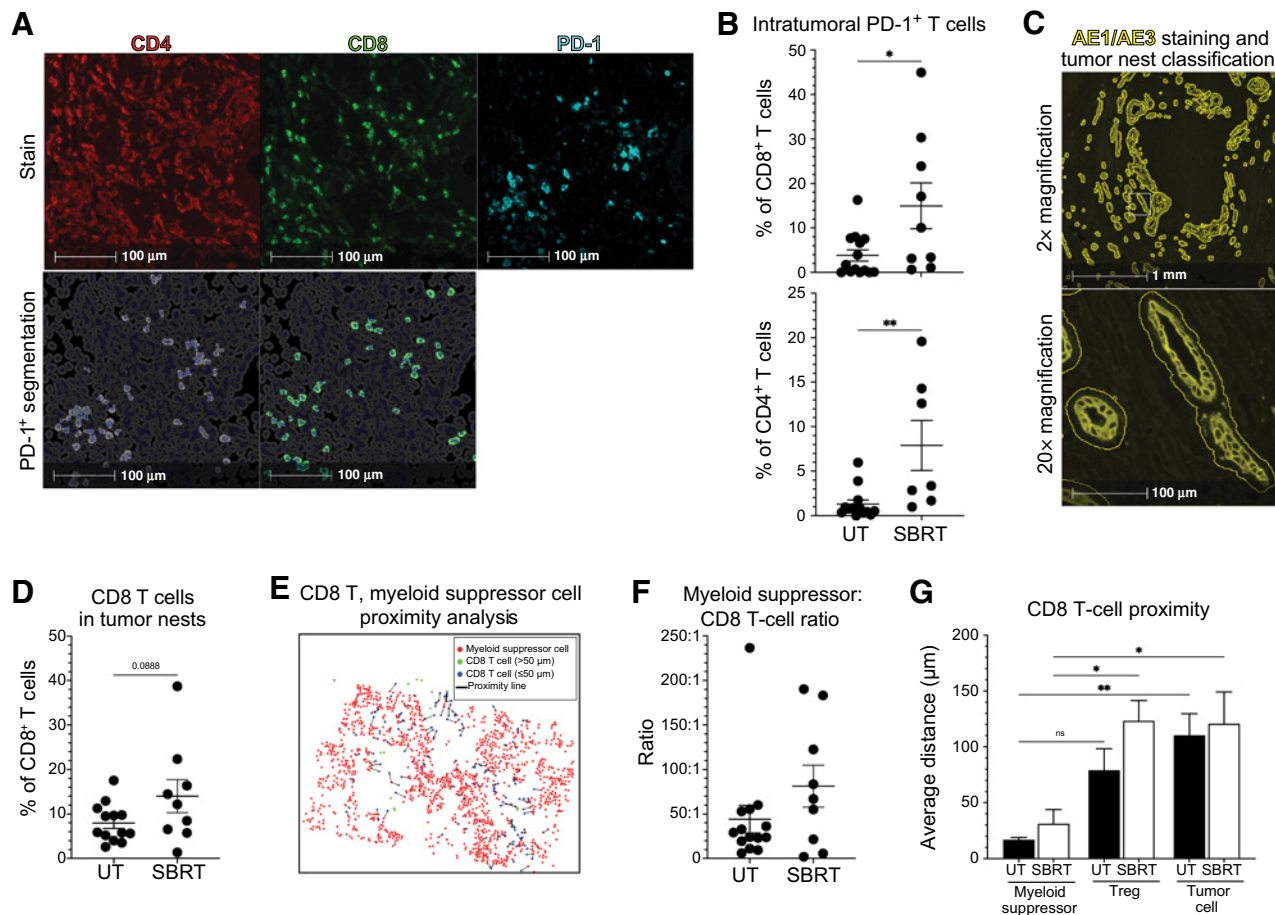
Figure 6.
T-cell activation in SBRT-treated PDAC contends with prevalent suppressor cell burden. **A** and **B**, PD-1⁺ CD8 and CD4 T cells were segmented from mIHC staining (**A**, representative images) for quantification as a percentage of total CD8 and CD4 T cells, respectively (**B**). **C** and **D**, Pan-cytokeratin (AE1/AE3) staining was used to annotate tumor nests using a tissue classifier machine learning algorithm (**C**, representative images), and percentages of CD8 T cells within tumor nests were quantified (**D**). Yellow lines annotate tumor nests. **E–G,** Proximity analysis of CD8 T cells, cumulative myeloid suppressor cells (monocytes, macrophages, granulocytes), Tregs, and tumor cells segmented from mIHC staining panels (**E**, representative plot) was used to quantify myeloid suppressor to CD8 T-cell ratios (**F**) and average distance between CD8 T cells and myeloid suppressors, Tregs, and tumor cells (**G**). Statistical significance was determined by unpaired parametric t-tests for cell ratio analysis, and two-way ANOVA (Tukey test) for average distance quantification. Data represent mean ± SEM (*, $P < 0.05$; **, $P < 0.01$). See also Supplementary Fig. S6.

effectors. This premise is further supported by increases in PD-1⁺ CD8 T cells observed in tumor regions following SBRT (revisit **Fig. 6**). Additional studies devoted to tracking CD8 T-cell migration between these regions in the context of SBRT are warranted.

A universal consequence of tumor irradiation is ancillary fibrosis, and accordingly, trichrome staining of SBRT-treated PDAC tissue demonstrated enhanced collagen deposition within days following treatment (revisit **Fig. 2**). Studies have suggested that the dense, desmoplastic stroma of PDAC may juxtatumorally sequester CD8 T cells and attenuate coordinated immune responses (56, 57). However, more recent work that comprehensively computed the spatial distribution of multiple cell types in the human PDAC TME using mIHC reported that desmoplasia did not appear to act as a physical barrier (58). Our findings corroborate the latter, as the enhanced collagen deposition that we observed in PDAC tissue following SBRT did not coincide with increased CD8 T-cell sequestration. Rather, our data suggest that augmentation of PD-L1 on PDAC cells is more likely a source of accessory immunosuppression driven by SBRT (revisit

Fig. 5). Type I and II IFN signaling induces PD-L1 expression during local inflammation to modulate acute responses and maintain peripheral tolerance (21, 44). Although we utilized PD-1 expression to (appropriately) classify activated CD8 T cells, we acknowledge that the PD-1⁺ subtype is paradoxically susceptible to exhaustion by TCR suppression and/or apoptosis via the PD-L1/PD-1 axis (59, 60). Preclinical studies as well as a recent phase I clinical trial have reported improved outcomes by combining radiotherapy and PD-L1 blockade for PDAC (61–63), and our findings support the further study of this immunotherapy combination for human disease.

Supplementing radiotherapy with PD-L1-targeted immunotherapy may improve therapeutic efficacy for PDAC; however, our findings indicate that more comprehensive interventions may be required for maximal benefit. Immune cells of both lymphoid (Treg) and myeloid (inflammatory monocyte, tumor-associated macrophage, granulocytic myeloid-derived suppressor cell) origins can further suppress antitumor immunogenicity. Our data suggest that SBRT alone may resolve lymphoid-driven immunosuppression, as both TLS and
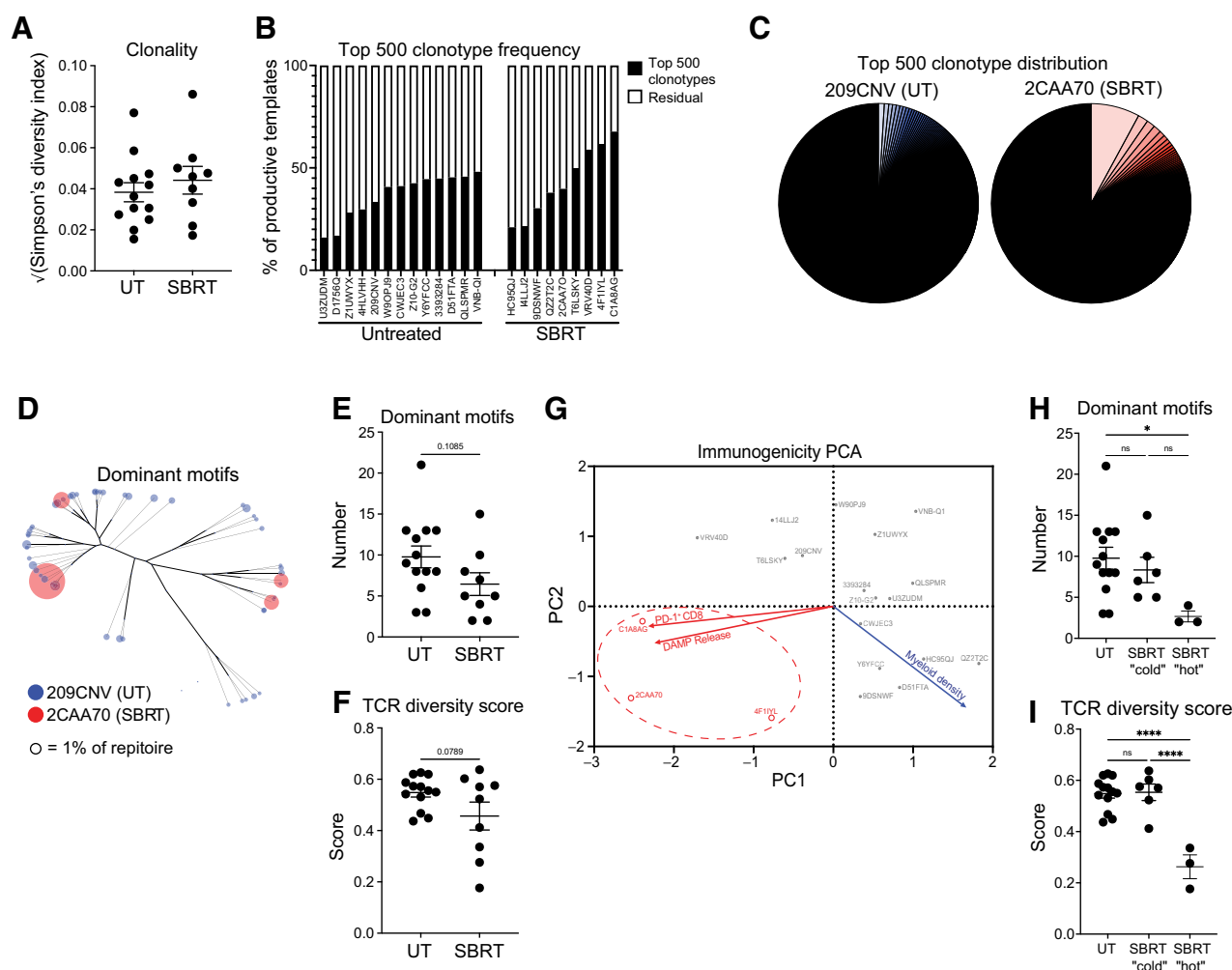
Figure 7.
SBRT induces clonal T-cell expansion in a subset of human PDAC tumors. **A–C,** TCR-seq was performed on whole PDAC sections to assess clonality (**A**) and clonotype frequency, presented cumulatively (**B**) and representatively (**C**) to demonstrate tumor-specific clonal responses. Statistical significance was determined by unpaired parametric t tests. **D–F,** ImmunoMap analysis was used to map dominant TCR motifs (**D**, representative dendrogram) for quantification (**E**) and diversity scoring (**F**). Statistical significance was determined by unpaired parametric t tests. **G–I,** PCA was used to cluster PDAC samples based on immunologic characteristics (arrows; **G**), and dominant motif number (**H**) and TCR diversity (**I**) were compared between immunologically "cold" and "hot" subsets. Red dotted line: "hot" subset. Statistical significance was determined by one-way ANOVA (Holm–Sidak test). All data represent mean ± SEM (*, $P < 0.05$; ****, $P < 0.0001$). See also Supplementary Fig. S6.

intratumoral Treg levels were found to be reduced following SBRT (revisit **Figs. 4** and **5**). However, immunosuppression in PDAC is most notably driven by a predominance of myeloid-derived suppressor cells, and therapeutically targeting this population via C-C chemokine receptor type 2 (CCR2) inhibition has been shown to improve PDAC patient outcomes (10, 64). Furthermore, work by Seifert and colleagues has demonstrated that radiotherapy recruits additional myeloid cells to the PDAC TME, and drives reprogramming toward a suppressive M2 phenotype by stimulating macrophage colony-stimulating factor (m-CSF) expression in PDAC cells (20). Although we did not observe augmented myeloid cell density or M2 polarization in the PDAC TME following SBRT, suppressor populations persisted and outnumbered CD8 T cells by nearly 100:1, likely contributing to T-cell anergy (revisit **Figs. 5** and **6**). This premise is supported by prior work reporting improved survival in resectable human PDAC following neoadjuvant FOLFIRINOX only in the setting of reduced M2 macrophage density (65). Complementary treatment strategies targeting

the suppressive myeloid component may be necessary to achieve durable therapeutic responses with SBRT in human PDAC.

The clinical study (NCT02347618) was designed to assess the safety and tolerability of neoadjuvant SBRT for patients with resectable PDAC; however, it was not powered to objectively correlate overall survival with SBRT responsivity at the cellular level, and further clinical studies with greater enrollment are warranted. Regardless, even with limited study cohorts, significant differences in the TME were observed following SBRT. Although no clinical features impacting the resection timeline were reported, analytical variability was likely introduced by the wide window of resection (12 days) post-SBRT. The days/weeks following tumor irradiation are extremely transient with respect to accumulating DNA damage and cell death, ECM conversion, and immune cell redistribution (37). A number of our findings may have been impacted by variable resection windows, such as TLS involvement and T-cell clonality. The relocation/reformation of TLS, and redistribution of stimulated T-cell repertoires

presumably takes weeks rather than days to manifest, and accordingly, ranging sample acquisition could lead to observations of reduced TLS and patient-specific T-cell clonal expansion, both of which were documented in this study. Nevertheless, no significant correlations were observed between time to resection and several of the radiologic/immunologic findings documented (data not shown).

Although radiotherapy does not generate robust therapeutic responses that profoundly impact PDAC patient outcomes, this work comprehensively examines the immunological impact of SBRT on the PDAC TME, and provides data supporting a role for SBRT in combination approaches. The patient cohort that received SBRT clearly demonstrated varying degrees of antitumor immunogenicity following treatment, with the most immunologically "hot" tumors possessing a unique clonal T-cell repertoire. Our characterization of the PDAC TME argues in support of antitumor immune priming initiated by SBRT, and identifies critical nodes of resistance that must be resolved to improve clinical outcomes. Accordingly, this work serves to educate the development of future immunotherapy strategies that target immunosuppressive features of the PDAC TME in coordination with SBRT delivery.

Authors' Disclosures

No disclosures were reported.

Authors' Contributions

B.N. Mills: Conceptualization, data curation, formal analysis, supervision, funding acquisition, investigation, visualization, methodology, writing–original draft, writing–review and editing. **H. Qiu:** Conceptualization, investigation, methodology, writing–review and editing. **M.G. Drage:** Resources, data curation, formal analysis, investigation, methodology, writing–review and editing. **C. Chen:** Data curation, formal analysis. **J.S. Mathew:** Data curation, formal analysis. **J. Garrett-Larsen:** Formal analysis. **J. Ye:** Methodology. **T.P. Uccello:** Data curation, formal analysis. **J.D. Murphy:** Writing–review and editing. **B.A. Belt:** Resources. **E.M. Lord:** Writing–review and editing. **A.W. Katz:** Conceptualization, resources. **D.C. Linehan:** Resources, funding acquisition, writing–review and editing. **S.A. Gerber:** Conceptualization, resources, supervision, funding acquisition, writing–review and editing.

Acknowledgments

Note

References

1. Cancer Facts & Figs. 2020. https://www.cancer.org/cancer/pancreatic-cancer/detection-diagnosis-staging/survival-rates.html#references.
2. Bayne LJ, Beatty GL, Jhala N, Clark CE, Rhim AD, Stanger BZ, et al. Tumor-derived granulocyte-macrophage colony-stimulating factor regulates myeloid inflammation and T cell immunity in pancreatic cancer. Cancer Cell 2012;21: 822–35.
3. Clark CE, Hingorani SR, Mick R, Combs C, Tuveson DA, Vonderheide RH. Dynamics of the immune reaction to pancreatic cancer from inception to invasion. Cancer Res 2007;67:9518–27.
4. Provenzano PP, Cuevas C, Chang AE, Goel VK, Von Hoff DD, Hingorani SR. Enzymatic targeting of the stroma ablates physical barriers to treatment of pancreatic ductal adenocarcinoma. Cancer Cell 2012;21:418–29.
5. Hiraoka N, Ino Y, Yamazaki-Itoh R, Kanai Y, Kosuge T, Shimada K. Intratumoral tertiary lymphoid organ is a favourable prognosticator in patients with pancreatic cancer. Br J Cancer 2015;112:1782–90.
6. Stromnes IM, Hulbert A, Pierce RH, Greenberg PD, Hingorani SR. T-cell localization, activation, and clonal expansion in human pancreatic ductal adenocarcinoma. Cancer Immunol Res 2017;5:978–91.
7. Sodergren MH, Mangal N, Wasan H, Sadanandam A, Balachandran VP, Jiao LR, et al. Immunological combination treatment holds the key to improving survival in pancreatic cancer. J Cancer Res Clin Oncol 2020;146: 2897–911.
8. Kamath SD, Kalyan A, Kircher S, Nimeiri H, Fought AJ, Benson A 3rd, et al. Ipilimumab and gemcitabine for advanced pancreatic cancer: a phase Ib study. Oncologist 2020;25:e808–15.
9. Ma J, Sun D, Wang J, Han C, Qian Y, Chen G, et al. Immune checkpoint inhibitors combined with chemotherapy for the treatment of advanced pancreatic cancer patients. Cancer Immunol Immunother 2020;69:365–72.
10. Nywening TM, Wang-Gillam A, Sanford DE, Belt BA, Panni RZ, Cusworth BM, et al. Targeting tumour-associated macrophages with CCR2 inhibition in combination with FOLFIRINOX in patients with borderline resectable and locally advanced pancreatic cancer: a single-centre, open-label, dose-finding, non-randomised, phase 1b trial. Lancet Oncol 2016;17:651–62.
11. Timke C, Winnenthal HS, Klug F, Roeder FF, Bonertz A, Reissfelder C, et al. Randomized controlled phase I/II study to investigate immune stimulatory effects by low dose radiotherapy in primarily operable pancreatic cancer. BMC Cancer 2011;11:134.
12. Giardino A, Innamorati G, Ugel S, Perbellini O, Girelli R, Frigerio I, et al. Immunomodulation after radiofrequency ablation of locally advanced pancreatic cancer by monitoring the immune response in 10 patients. Pancreatology 2017;17:962–6.
13. Pandit H, Hong YK, Li Y, Rostas J, Pulliam Z, Li SP, et al. Evaluating the regulatory immunomodulation effect of irreversible electroporation (IRE) in pancreatic adenocarcinoma. Ann Surg Oncol 2019;26:800–6.
14. Timmerman RD, Herman J, Cho LC. Emergence of stereotactic body radiation therapy and its impact on current and future clinical practice. J Clin Oncol 2014; 32:2847–54.
15. Wu G, Baine MJ, Zhao N, Li S, Li X, Lin C. Lymphocyte-sparing effect of stereotactic body radiation therapy compared to conventional fractionated radiation therapy in patients with locally advanced pancreatic cancer. BMC Cancer 2019;19:977.
16. Gerber SA, Sedlacek AL, Cron KR, Murphy SP, Frelinger JG, Lord EM. IFN-gamma mediates the antitumor effects of radiation therapy in a murine colon tumor. Am J Pathol 2013;182:2345–54.
17. Ye J, Mills BN, Zhao T, Han BJ, Murphy JD, Patel AP, et al. Assessing the magnitude of immunogenic cell death following chemotherapy and irradiation reveals a new strategy to treat pancreatic cancer. Cancer Immunol Res 2020; 8:94–107.
18. Kachikwu EL, Iwamoto KS, Liao YP, DeMarco JJ, Agazaryan N, Economou JS, et al. Radiation enhances regulatory T cell representation. Int J Radiat Oncol Biol Phys 2011;81:1128–35.
19. Kozin SV, Kamoun WS, Huang Y, Dawson MR, Jain RK, Duda DG. Recruitment of myeloid but not endothelial precursor cells facilitates tumor regrowth after local irradiation. Cancer Res 2010;70:5679–85.
20. Seifert L, Werba G, Tiwari S, Giao Ly NN, Nguy S, Alothman S, et al. Radiation therapy induces macrophages to suppress T-cell responses against pancreatic tumors in mice. Gastroenterology 2016;150:1659–72.
21. Dovedi SJ, Adlard AL, Lipowska-Bhalla G, McKenna C, Jones S, Cheadle EJ, et al. Acquired resistance to fractionated radiotherapy can be overcome by concurrent PD-L1 blockade. Cancer Res 2014;74:5458–68.

22. Zhong J, Patel K, Switchenko J, Cassidy RJ, Hall WA, Gillespie T, et al. Outcomes for patients with locally advanced pancreatic adenocarcinoma treated with stereotactic body radiation therapy versus conventionally fractionated radiation. Cancer 2017;123:3486–93.

23. Subramanian A, Tamayo P, Mootha VK, Mukherjee S, Ebert BL, Gillette MA, et al. Gene set enrichment analysis: a knowledge-based approach for interpreting genome-wide expression profiles. Proc Natl Acad Sci U S A 2005;102:15545–50.

24. Liberzon A, Subramanian A, Pinchback R, Thorvaldsdottir H, Tamayo P, Mesirov JP. Molecular signatures database (MSigDB) 3.0. Bioinformatics 2011;27:1739–40.

25. Liberzon A, Birger C, Thorvaldsdottir H, Ghandi M, Mesirov JP, Tamayo P. The molecular signatures database (MSigDB) hallmark gene set collection. Cell Syst 2015;1:417–25.

26. Amundson SA, Do KT, Vinikoor L, Koch-Paiz CA, Bittner ML, Trent JM, et al. Stress-specific signatures: expression profiling of p53 wild-type and -null human cells. Oncogene 2005;24:4572–9.

27. Warters RL, Packard AT, Kramer GF, Gaffney DK, Moos PJ. Differential gene expression in primary human skin keratinocytes and fibroblasts in response to ionizing radiation. Radiat Res 2009;172:82–95.

28. Liao Y, Wang J, Jaehnig EJ, Shi Z, Zhang B. WebGestalt 2019: gene set analysis toolkit with revamped UIs and APIs. Nucleic Acids Res 2019;47:W199–205.

29. Sidhom JW, Bessell CA, Havel JJ, Kosmides A, Chan TA, Schneck JP. ImmunoMap: a bioinformatics tool for T-cell repertoire analysis. Cancer Immunol Res 2018;6:151–62.

30. Aubrey BJ, Kelly GL, Janic A, Herold MJ, Strasser A. How does p53 induce apoptosis and how does this relate to p53-mediated tumour suppression? Cell Death Differ 2018;25:104–13.

31. Adjemian S, Oltean T, Martens S, Wiernicki B, Goossens V, Vanden Berghe T, et al. Ionizing radiation results in a mixture of cellular outcomes including mitotic catastrophe, senescence, methuosis, and iron-dependent cell death. Cell Death Dis 2020;11:1003.

32. Fucikova J, Moserova I, Urbanova L, Bezu L, Kepp O, Cremer I, et al. Prognostic and predictive value of DAMPs and DAMP-associated processes in cancer. Front Immunol 2015;6:402.

33. Jang GY, Lee JW, Kim YS, Lee SE, Han HD, Hong KJ, et al. Interactions between tumor-derived proteins and Toll-like receptors. Exp Mol Med 2020; 52:1926–35.

34. Yarnold J, Brotons MC. Pathogenetic mechanisms in radiation fibrosis. Radiother Oncol 2010;97:149–61.

35. Watanabe I, Hasebe T, Sasaki S, Konishi M, Inoue K, Nakagohri T, et al. Advanced pancreatic ductal cancer: fibrotic focus and beta-catenin expression correlate with outcome. Pancreas 2003;26:326–33.

36. Neesse A, Michl P, Frese KK, Feig C, Cook N, Jacobetz MA, et al. Stromal biology and therapy in pancreatic cancer. Gut 2011;60:861–8.

37. Barker HE, Paget JT, Khan AA, Harrington KJ. The tumour microenvironment after radiotherapy: mechanisms of resistance and recurrence. Nat Rev Cancer 2015;15:409–25.

38. Langley RE, Bump EA, Quartuccio SG, Medeiros D, Braunhut SJ. Radiation-induced apoptosis in microvascular endothelial cells. Br J Cancer 1997;75: 666–72.

39. Roth S, Zamzow K, Gaida MM, Heikenwalder M, Tjaden C, Hinz U, et al. Evolution of the immune landscape during progression of pancreatic intraductal papillary mucinous neoplasms to invasive cancer. EBioMedicine 2020;54: 102714.

40. Colbeck EJ, Ager A, Gallimore A, Jones GW. Tertiary lymphoid structures in cancer: Drivers of antitumor immunity, immunosuppression, or bystander sentinels in disease? Front Immunol 2017;8:1830.

41. Xu J, Escamilla J, Mok S, David J, Priceman S, West B, et al. CSF1R signaling blockade stanches tumor-infiltrating myeloid cells and improves the efficacy of radiotherapy in prostate cancer. Cancer Res 2013;73:2782–94.

42. Murakami S, Shahbazian D, Surana R, Zhang W, Chen H, Graham GT, et al. Yes-associated protein mediates immune reprogramming in pancreatic ductal adenocarcinoma. Oncogene 2017;36:1232–44.

43. Birnbaum DJ, Finetti P, Lopresti A, Gilabert M, Poizat F, Turrini O, et al. Prognostic value of PDL1 expression in pancreatic cancer. Oncotarget 2016;7: 71198–210.

44. Deng L, Liang H, Burnette B, Beckett M, Darga T, Weichselbaum RR, et al. Irradiation and anti-PD-L1 treatment synergistically promote antitumor immunity in mice. J Clin Invest 2014;124:687–95.

45. Lhuillier C, Rudqvist NP, Yamazaki T, Zhang T, Charpentier M, Galluzzi L, et al. Radiotherapy-exposed CD8+ and CD4+ neoantigens enhance tumor control. J Clin Invest 2021;131:e138740.

46. Chow J, Hoffend NC, Abrams SI, Schwaab T, Singh AK, Muhitch JB. Radiation induces dynamic changes to the T cell repertoire in renal cell carcinoma patients. Proc Natl Acad Sci U S A 2020;117:23721–9.

47. Rudqvist NP, Pilones KA, Lhuillier C, Wennerberg E, Sidhom JW, Emerson RO, et al. Radiotherapy and CTLA-4 blockade shape the TCR repertoire of tumor-infiltrating T cells. Cancer Immunol Res 2018;6:139–50.

48. Gerber SA, Lim JY, Connolly KA, Sedlacek AL, Barlow ML, Murphy SP, et al. Radio-responsive tumors exhibit greater intratumoral immune activity than nonresponsive tumors. Int J Cancer 2014;134:2383–92.

49. Garcia-Barros M, Paris F, Cordon-Cardo C, Lyden D, Rafii S, Haimovitz-Friedman A, et al. Tumor response to radiotherapy regulated by endothelial cell apoptosis. Science 2003;300:1155–9.

50. Moeller BJ, Dreher MR, Rabbani ZN, Schroeder T, Cao Y, Li CY, et al. Pleiotropic effects of HIF-1 blockade on tumor radiosensitivity. Cancer Cell 2005;8:99–110.

51. Song CW, Park I, Cho LC, Yuan J, Dusenbery KE, Griffin RJ, et al. Is indirect cell death involved in response of tumors to stereotactic radiosurgery and stereotactic body radiation therapy? Int J Radiat Oncol Biol Phys 2014;89:924–5.

52. Song CW, Cho LC, Yuan J, Dusenbery KE, Griffin RJ, Levitt SH. Radiobiology of stereotactic body radiation therapy/stereotactic radiosurgery and the linear-quadratic model. Int J Radiat Oncol Biol Phys 2013;87:18–9.

53. Kim MS, Kim W, Park IH, Kim HJ, Lee E, Jung JH, et al. Radiobiological mechanisms of stereotactic body radiation therapy and stereotactic radiation surgery. Radiat Oncol J 2015;33:265–75.

54. Song CW, Lee YJ, Griffin RJ, Park I, Koonce NA, Hui S, et al. Indirect tumor cell death after high-dose hypofractionated irradiation: implications for stereotactic body radiation therapy and stereotactic radiation surgery. Int J Radiat Oncol Biol Phys 2015;93:166–72.

55. Moding EJ, Castle KD, Perez BA, Oh P, Min HD, Norris H, et al. Tumor cells, but not endothelial cells, mediate eradication of primary sarcomas by stereotactic body radiation therapy. Sci Transl Med 2015;7:278ra34.

56. Ene-Obong A, Clear AJ, Watt J, Wang J, Fatah R, Riches JC, et al. Activated pancreatic stellate cells sequester CD8+ T cells to reduce their infiltration of the juxtatumoral compartment of pancreatic ductal adenocarcinoma. Gastroenterology 2013;145:1121–32.

57. Feig C, Jones JO, Kraman M, Wells RJ, Deonarine A, Chan DS, et al. Targeting CXCL12 from FAP-expressing carcinoma-associated fibroblasts synergizes with anti-PD-L1 immunotherapy in pancreatic cancer. Proc Natl Acad Sci U S A 2013; 110:20212–7.

58. Carstens JL, Correa de Sampaio P, Yang D, Barua S, Wang H, Rao A, et al. Spatial computation of intratumoral T cells correlates with survival of patients with pancreatic cancer. Nat Commun 2017;8:15095.

59. Freeman GJ, Long AJ, Iwai Y, Bourque K, Chernova T, Nishimura H, et al. Engagement of the PD-1 immunoinhibitory receptor by a novel B7 family member leads to negative regulation of lymphocyte activation. J Exp Med 2000; 192:1027–34.

60. Dong H, Strome SE, Salomao DR, Tamura H, Hirano F, Flies DB, et al. Tumor-associated B7-H1 promotes T-cell apoptosis: a potential mechanism of immune evasion. Nat Med 2002;8:793–800.

61. Azad A, Yin Lim S, D'Costa Z, Jones K, Diana A, Sansom OJ, et al. PD-L1 blockade enhances response of pancreatic ductal adenocarcinoma to radiotherapy. EMBO Mol Med 2017;9:167–80.

62. Chuong M, Chang ET, Choi EY, Mahmood J, Lapidus RG, Davila E, et al. Exploring the concept of radiation "Booster Shot" in combination with an anti-PD-L1 mAb to enhance anti-tumor immune effects in mouse pancreas tumors. J Clin Oncol Res 2017;5:1058.

63. Xie C, Duffy A, Brar G, Fioravanti S, Mabry-Hrones D, Walker M, et al. Immune checkpoint blockade in combination with stereotactic body radiotherapy in patients with metastatic pancreatic ductal adenocarcinoma. Clin Cancer Res 2020;26:2318–26.

64. Sanford DE, Belt BA, Panni RZ, Mayer A, Deshpande AD, Carpenter D, et al. Inflammatory monocyte mobilization decreases patient survival in pancreatic cancer: a role for targeting the CCL2/CCR2 axis. Clin Cancer Res 2013;19: 3404–15.

65. Michelakos T, Cai L, Villani V, Sabbatino F, Kontos F, Fernandez-Del Castillo C, et al. Tumor microenvironment immune response in pancreatic ductal adeno-carcinoma patients treated with neoadjuvant therapy. J Natl Cancer Inst 2021; 113:182–91.